J. Jpn. Soc. Powder Powder Metallurgy, **72** (2025) S91-S97
https://doi.org/10.2497/jjspm.14B-T6-07

Exploring the Influence of PBF-LB/M Process Parameters in Multi-Material AM: a Single-Track Study on CuCrZr Deposited onto IN718 Substrate

José Manuel CREGO LOZARES[1,2]*, Alexander E. MEDVEDEV[1], Karim ASAMI[2] Claus EMMELMANN[2], Andrey MOLOTNIKOV[1] and Milan BRANDT[1]

1, RMIT Centre for Additive Manufacturing, Royal Melbourne Institute of Technology, School of Engineering, 3053 VIC, Australia.

2, Institute of Laser and System Technologies, Hamburg University of Technology, Harburger Schloßstraße 28, 21079 Hamburg, Germany.

Abstract:

In the context of multi-material additive manufacturing (MMAM), Cu-based alloys present inherent chemical and physical properties mismatch with other alloys that often lead to cracking, dimensional mismatch and poor bond performance at the interface. This, combined with the lack of optimized laser parameters for the desired arrangement of materials in the 3D-space present a challenge to achieve functionally distinct regions. IN718, which has been used in the past together with Cu-based alloys, benefits from great chemical affinity of Ni with Cu and, and contrary to 316L, has been rarely explored with Cu alloys in PBF-LB/M. The present work focuses on the feasibility study of printing CuCrZr onto IN718 substrate and the influence of PBF-LB/M process parameters on the morphology and the composition of the meltpool. CuCrZr single tracks were printed onto IN718 buildplate for different set of process parameters including laser power, scan speed and layer thickness.

Keywords: Multi-material, Functionally Graded Material, PBF-LB/M, CuCrZr, IN718

Introduction

Established as one of the pioneering copper-based alloys in aerospace sector, CuCrZr (C-18150) inspires great interest in applications where heat dissipation is key. Its improved strength on top of an excellent thermal conductivity makes this alloy a promising candidate material for regeneratively-cooled combustion chambers components, like liners (1). Nevertheless, these chambers require a thermal jacket that can withstand the radial and axial loads during operation (2). This jacket is typically made from a high strength-to-weight ratio material, such as nickel-based superalloy IN625 or NASA HR-1, and is fabricated through a separate additive manufacturing (AM) step, such as WAAM, DED or cold spray (3) due to the ease of deposition when aided by the robotic gantry arm (4). Despite a substantial amount of attention to this method (5), it also comes with notable limitations, including multiple fabrication stages, difficulty to perform surface/part checks and, specifically for DED process, undesired shrinkage effects in the overall part and defect formation around the interface as a result of the high energy input (3). These defects are typically linked to the difference in thermal properties (melting temperature, thermal expansion coeficient (CTE) and thermal conductivity k) and hot cracking during solidification. In this context, functional grading between two materials could be a promising strategy to mitigate the formation of such defects. Through the use of intermediate composition layers or the use of an intermediate material, it is possible to attenuate the change in thermal properties, thereby obtaining a smooth transition between the two alloys (6).

While DED fabrication methods have a unique advantage for creating compositional gradients thanks to the independent powder feeds that allow for controlled in-situ mixing (4), large spot size and high energy input put notable limitations on the design, fabrication and quality control of multi-material interfaces. Recent advances in the multi-material powder bed fusion methods (PBF-LB/M) provide an existing alternative to DED processes due to a more precise process and geometry control, both in the bulk and around the multi-material interfaces (7). However, process optimization for multi-material PBF-LB/M is in its infancy, and process assessment and analysis are needed to ensure suitable parameters for the specific materials combinations and their three-dimensional arrangement.

According to literature, the vast majority of recent efforts focused on the CuCrZr/316L combination, both as a part of single- and multi-material powder bed systems (7–13). At the same time, the copper alloy has rarely been paired with IN718 in PBF-LB/M process, even though the Ni-based superalloy provides a benefit of excellent chemical compatibility with CuCrZr. The available literature only provides a rough assessment of the feasibility and manufacturability of CuCrZr/IN718 combination, with limited assessment of process optimization and/or metallurgical analysis of the interface region. For example, Marques et al. studied the feasibility to manufacture vertical heat-conducting channels of pure Cu within IN718 with a custom MMAM PBF-LB/M system (14) and through a powder technology route where Cu cooling channels proved an increment of 25% of thermal conductivity when compared to bulk IN718 (15). Aiming to diminish the diffusion of copper into steel, Li et al. explored the use of IN718 as an intermediate material for joining 316L and CuCrZr reducing the strain between IN718 and CuCrZr (16). However, no specific attention has been given to the selection of the process parameters to achieve a better bonding between the two different alloys. The present paper focuses on studying the influence of the PBF-LB/M process parameters on the characteristics of CuCrZr alloy single tracks deposited onto IN-718 substrate with special focus on their three-dimensional morphology and chemical composition to evaluate the selected process window for optimized manufacturability and powder conversion efficiency. Crucially, the focus on the single tracks is expected to provide an initial assessment of the process to inform its subsequent optimization for our future multi-track and multi-layer experiments.

*corresponding author, E-mail: jose.lozares@tuhh.de

Experiment

CuCrZr gas atomized powder used in this study was acquired from Eckart TLS GmbH (Germany) with D10=6.09µm, D50=21.67µm, and D90=35.39µm, and sieved with a 25µm sieve to D10=18.49µm, D50=28.84µm, and D90=39.12µm. Annealed IN-718 plates with dimensions 15mmx15mmx4mm were purchased from Austral Wright Metals (Melbourne, Victoria, Australia) and machined to BP dimensions. The chemical composition and of powder and the build plate are listed in Table 1.

Table 1. Chemical composition of CuCrZr powder and IN718 substrate

Wt.%	**Fe**	**Cu**	**Ni**	**Cr**	**Zr**	**Mo**	**Nb**	**Al**	**Ti**	**Co**
CuCrZr	-	Bal.	-	1.0	0.3	-	-	-	-	-
IN-718	Bal.	-	55	17	-	2.8	4.9	0.5	0.9	0.3

Manufacturing of the CuCrZr single tracks was carried out in an Aconity MIDI+ powder bed fusion system (Aconity GmbH, Aachen, Germany) equipped with a Gaussian beam source with a maximum power of 800W and a minimum spot size of 80 µm (alta Fiber Laser, nLIGHT). In order to determine the influence of the laser parameters, a full factorial Design of Experiments (DOE) was carried out for different laser power, scan speed, and layer thickness. Initial parameters were chosen based on previous single material DOE literature (12,17) that indicated the potential suitable process parameter window. The parameters chosen are listed in Table 2.

Table 2. Laser parameters used for single tracks DOE

Scan speed, v_{scan} (mm/s)	**Laser Power, P_{Laser} (J/mm^3)**	**Layer thickness, d (µm)**	**Spot Diameter, ϕ (µm)**
500, 750, 1000	500, 650, 800	30, 60, 90	135

To assess the three-dimensional morphology of single tracks, their average width as well as depth and deposition height have been measured. The width of the tracks was measured in 10 randomized points along the tracks using Keyence VHX-5000 (Keyence, Japan) optical microscope (OM). For melt pool depth and deposition height measurements, three cross sections segments per single track were obtained from the substrate using EDM wire cutting and cleaned in an ultrasonic bath with ethanol. The cross sections underwent metallographic preparation including SiC 500 followed by 2 different diamond polishing suspensions and final polishing with 0.04µm colloidal silica suspension. A total of 3 equidistant cross sections per track were explored using Keyence VHX-5000 to determine the depth and height of the meltpool. SEM and EDS analysis were performed with a JEOL 7200 F Schottky field emission scanning electron microscope (SEM) (JEOL Ltd., Tokyo, Japan) at an accelerating voltage of 10kV and an emission current of 70nA, equipped with energy dispersive spectroscopy (EDS) detector (Oxford Instruments).

Results and Discussion

For this study, the tracks topology was classified into different categories taking previous work as a reference (18,19). Depending on the track continuity and the dimensions of the cross sections, the tracks were classified into the following categories shown in Fig. 1:

1. Conduction (green square). Continuous track with homogeneous width and clearly defined boundaries.
2. Keyhole (red square). Continuous track with homogeneous width and clearly defined boundaries with depth-over-width ratio D/w>0.8 according to (20).
3. Protrusion and depression (yellow circle). This topology is characterized by depression regions on both sides of the weld bead. Long meltpools formed due to increased backward flow caused by intense Marangoni flow and vaporization pressure are directly associated to this topology (21). As a result of the Plateau-Rayleigh instability, a protrusion is formed in the middle of the track that solidifies before breaking into single melt balls (22,23).
4. Humping (blue circle). The track is characterized by a continuous profile that periodically accumulates material. As a result of Plateau Rayleigh instability, material accumulates forming protrusions before allowing the formation of individual balls (23,24).

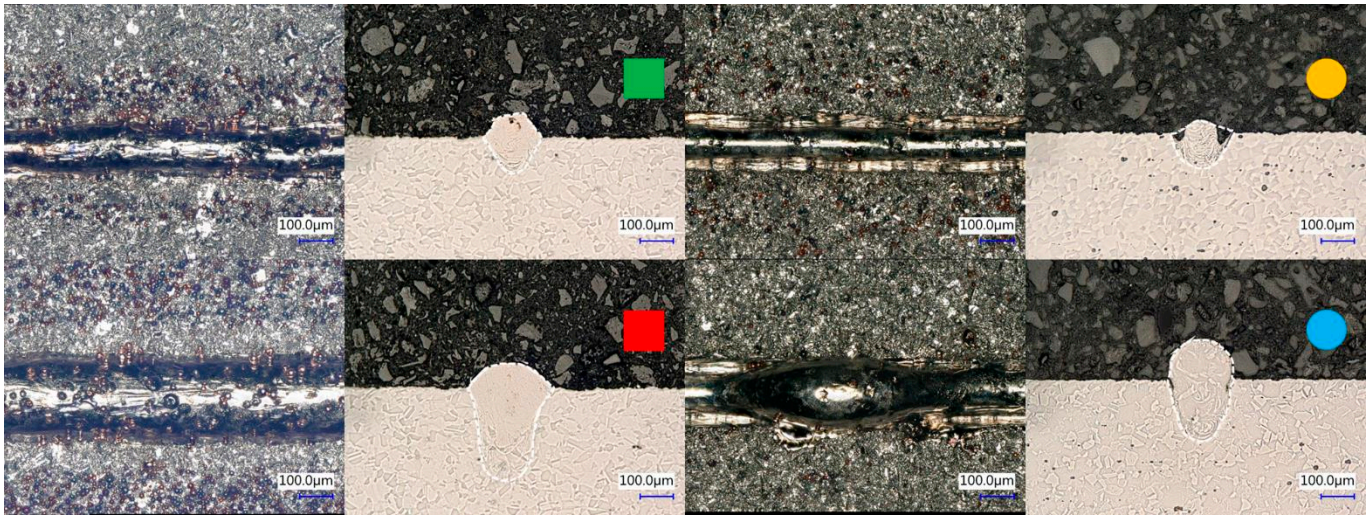

Fig. 1. Overview of different types of tracks with close detail and cross section.

The main goal of the DOE is to find the best processing parameters. Fig. 2 collects the classification of the single tracks for different *d*. For better understanding of the tendencies of the meltpool dimensions, these parameters can be easily tracked as a function of the Linear Energy Density (LED):

$$LED = \frac{P_{Laser}}{v_{scan}}$$

where P_{Laser} is the laser power supplied by the laser, and v_{scan} is the scan speed. The results reveal different characteristics of the meltpool development in response to the variation of the process parameters. Keyhole formation is achieved in the majority of the studied configurations due to the high energy input. A selection of process parameters with low energy density is necessary to avoid keyhole mode. For the 3 values of *d* explored the single tracks show continuity configurations at 500 and 750mm/s, and discontinuities associated to humping are detected for higher scan speeds as shown in Fig. 2. Configurations with the highest scan speed of 1000mm/s and laser power 500 and 650W present protrusion and depression condition previously reported by (18), for 30µm. Tracks manufactured at 1000mm/s and 800W presented humping for *d*=30 and 60µm. In previous studies on single material, the gaussian mode shows this behavior at high laser powers and scan speeds (19). In this study, configurations that achieved humping topology reveal a similar cross section as the protrusion and depression, however the depth is too prominent. These depressions were easily detected during the top-view exploration of the single tracks and there are less frequent as the *d* increases.

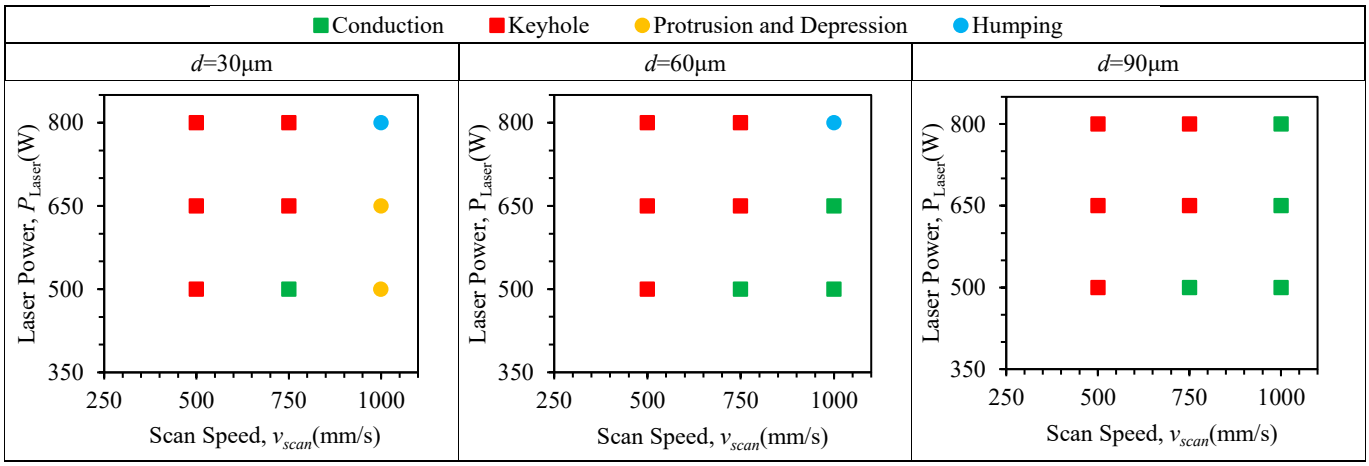

Fig. 2. Laser Power(P_{Laser}) – Scan Speed(v_{scan}) process map for layer thickness *d*=30-(left), 60-(middle), and 90-micron(right) layer thickness of single-track experiments of CuCrZr onto IN718 substrate.

Fig. 3 depicts the width, penetration depth and height of the single tracks for different layer thicknesses 30µm(black)(left), 60µm(orange)(middle), and 90 µm(blue)(right) as function of LED. One can see that the change in width of the tracks is minimal regardless of the value of *d* chosen. The minimum width achieved for the gaussian spot size is 158.46±10.20µm(500W, 750mm/s), which is 17.4% higher than the nominal laser spot size(135um). It can also be seen that the meltpool penetration into the substrate dramatically increases for higher energy density. Height measurements in for every *d* reveal that the control over the height of the track is not as stable as the width. Inevitably,

the cross sections explored for 800W and 1000mm/s at *d*=30µm are treated as an outlier as the values are exceptionally high. The measurements taken for this configuration do coincide with humps in the track leading to a non-reliable measurement. Single tracks manufactured with *d*=30 µm show stable heights within the 20% deviation for the 500W configurations and exceptionally for the configuration at 650W and 750mm/s(34.27±1.42 µm). A similar trend is observed for *d*=60µm with the most accurate value 62.87±20.32µm(500W, 750mm/s). The trend disappears for *d*=90 µm showing that only the configurations 800W at 1000mm/s(94±41.35 µm) and 650W at 500mm/s(92±19.22 µm) are within the 5% deviation. The height measurements reveal that there is some incompatibility between the desired height of the single track and the behaviour, making this parameter another restriction to be considered for the processing parameter window.

The findings from Fig. 2 and Fig. 3 indicate that the energy density window chosen based on the literature search is not optimal as the tracks tend to fall into keyhole mode quite easily, even for *d*=90µm. Moreover, only a few configurations are able to provide an average track height near the desired value which imposes additional limitations for selecting process parameters for manufacturing an actual part. Nevertheless, this finding is highly useful in informing our planned future work on larger scale samples (rather than single tracks), where we will explore a larger parameter space to optimise manufacturability as well as microstructure and mechanical properties of the multi-material interface between CuCrZr and IN718.

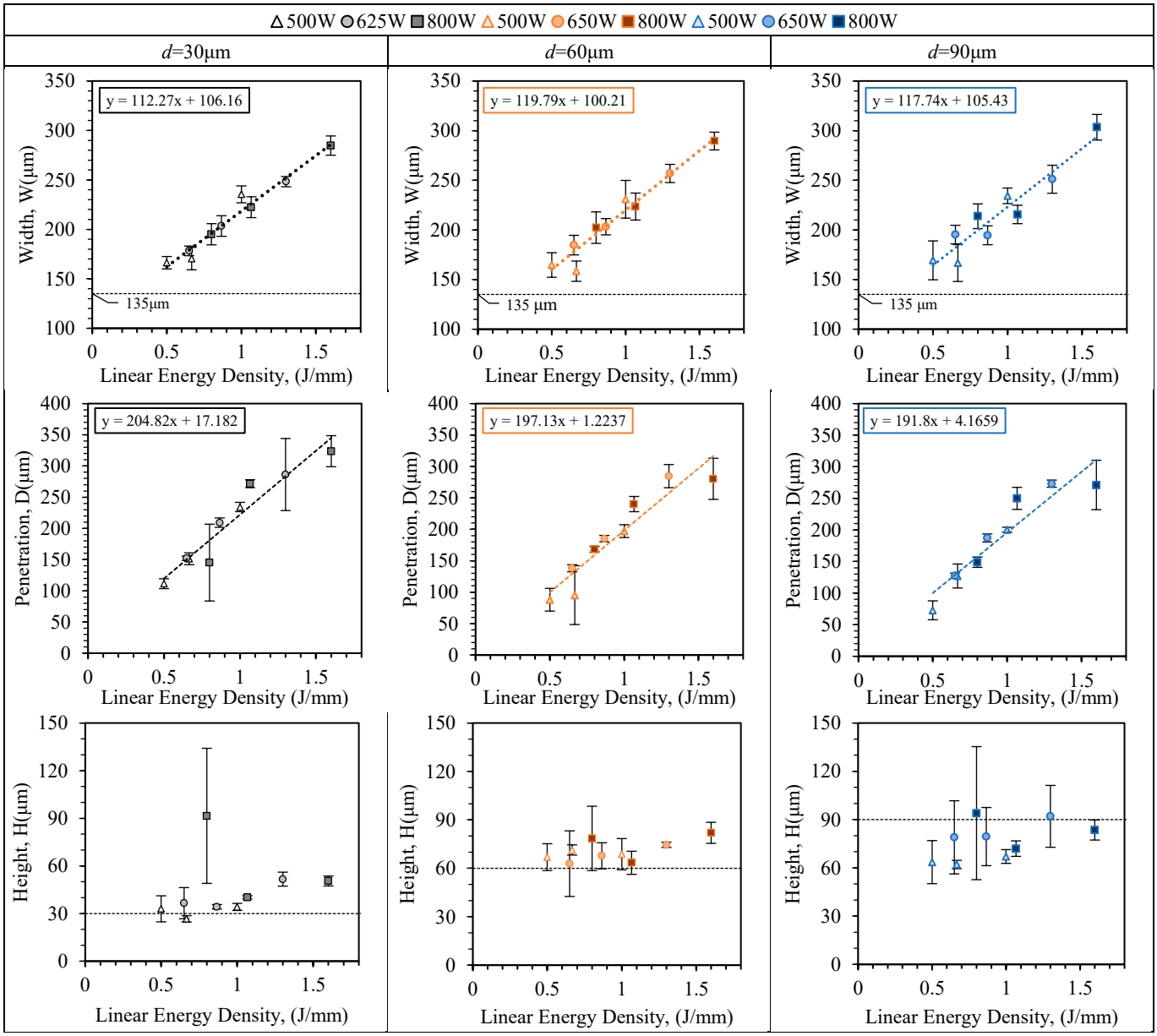

Fig. 3. Average values for Width, Depth and Height of meltpool 30µm(black)(left), 60 µm(orange)(middle) and 90µm(blue)(right) for different process parameters with linear fitting curves.

Even though keyhole mode governs the majority of the explored configurations, selected parameter window presents continuity and good control over track width. Further exploration of smaller LED configurations will secure smaller meltpool width and lower penetration at the

expense of track continuity due to lack of sustained energy. As it can be seen in Fig. 1, the overall cross section shows a color more similar to the substrate than to the characteristic reddish tone from the Cu-based alloy, leaving only small regions of CuCrZr noticeable. In order to assess the bond quality between the deposited CuCrZr and the IN718 substrate, the cross sections were examined at SEM for compositional analysis.

Cu-based powders are notorious for posing difficulties during laser-based manufacturing processes due to high reflectivity, low laser absorptivity and therefore a limited manufacturability when working with near-infrared lasers (25,26). For this reason, it is important to evaluate the effect of process parameter optimization on the powder conversion into molten state during fabrication. We used the Cu Wt.%(accounting for 98.8Wt.% in CuCrZr powder) in the meltpool as an indicator of the retained Cu inside the meltpool. Fig. 4(up) shows an example of the EDS mapping of the single track printed at 500W, 1000mm/s and 60µm. Notice that the Zr map as well as other elements below 1 Wt.% are not present due to small traceability. Three EDS measurements with sigma error σ=1 were taken in each of the 3 cross sections for statistical purposes. Fig. 4(left) show the average Cu Wt.% composition of the cross section of 5 different energy densities configurations.

The EDS characterization of the melt pool cross sections revealed some trends in the retained amount of CuCrZr in the meltpool. Overall the maps reveal a positive trend on the Cu Wt.% with the increase in layer thickness *d*. Considering all the linear energy configurations studied, the Cu Wt.% process window can guarantee a value between 43.07±2.4 and 5.50±0.37 by changing the P_{Laser} and v_{Scan} for the different layer thicknesses as seen in Fig. 4(left). Cu Wt.% for 60µm is 246.31% higher than 30µm on average for energy densities above 0.8 J/mm, while an increment between 60 and 90µm is not clear. As we decrease the energy density from 0.8 J/mm, the transition from conduction to keyhole diminishes drastically the area, affecting both the distribution and concentration of the deposited CuCrZr. Configurations with the lower energy density show the highest content in Cu Wt.% being 43.07±2.4, 39.70±0.3 and 13.07±0.3 for 90, 60 and 30µm respectively.

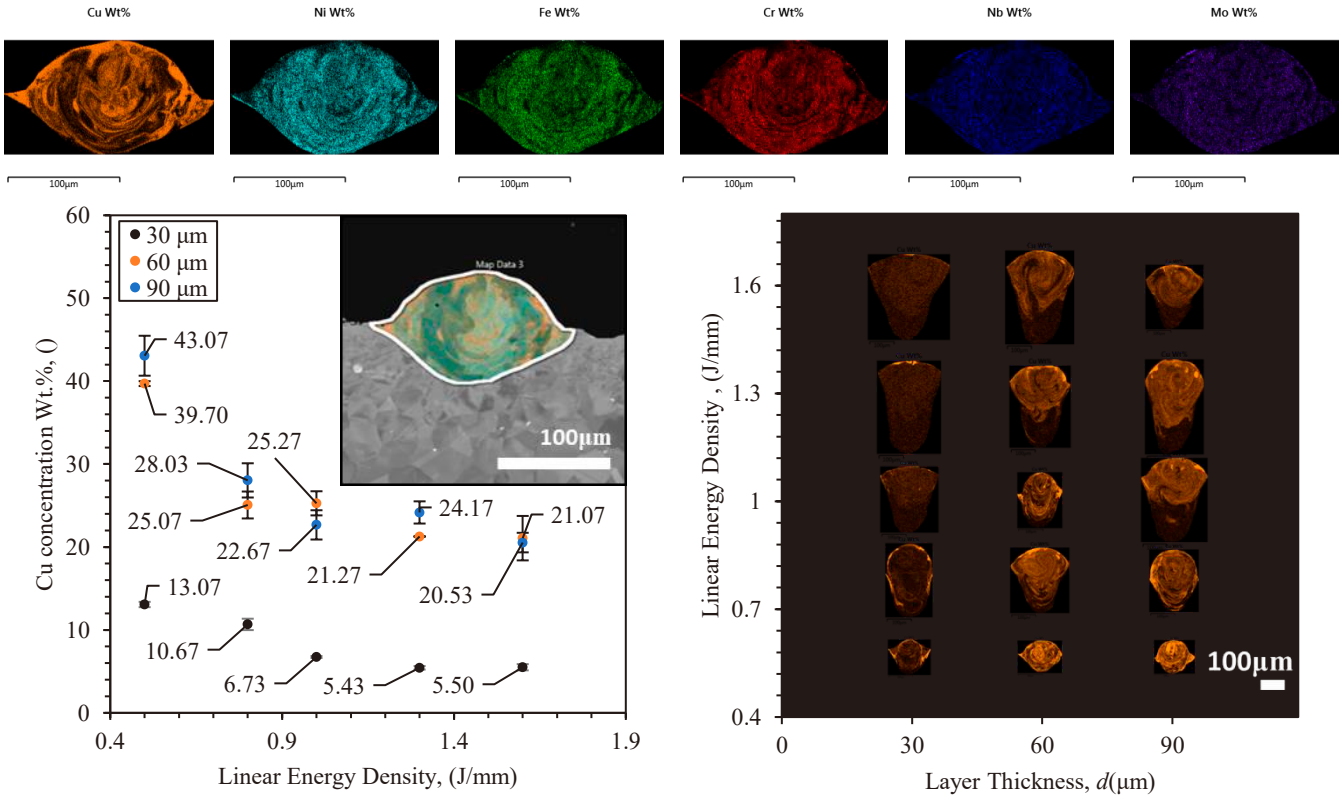

Fig. 4. EDS maps for example track(up), average Cu Wt.%(left), and Cu Wt.% EDS maps(right) shorted by LED and d.

All characterized cross sections in Fig. 4(right) reveal a higher concentration of Cu in the top and side regions of the bead. This accumulation of CuCrZr was previously reported by Mao et al. (27) when simulating the PBF-LB/M of CuCrZr onto 316L where the high Marangoni forces and the recoil pressure from the PBF-LB/M were identified as the main influencing factors. Besides these accumulations, the distribution is homogeneous for *d*=30µm. Cross sections for *d*=60 and 90µm reveal a distinct boundary between the upper region of the meltpool and the lower region linked to the keyhole effect. The location of the Cu in this upper region could be associated with the original location of the deposited alloy as well as the Marangoni effect only allowing a small amount of Cu to go below this boundary. For the same laser power, this effect is diminished for higher scan speeds as it can be seen for the configurations of 0.8J/mm and 1.6J/mm. For configurations with the same scan speed, a decrease in laser power will only show small variations when within the keyhole regime.

Although further complimentary characterization needs to be done to support the results reported from EDS measurements, clear trends in the Wt.% can be observed for the different configurations explored. Aiming to determine the efficiency of the deposition of the CuCrZr, EDS

maps reveal a pattern for the LED supplied. The average value of Cu Wt.% found inside the meltpool area translates into a potential indicator of the rich Cu-based alloy deposited up to a certain value of layer thickness. Even though the Cu Wt.% is expected to increase for lower energy density configurations, these changes in LED present themselves unrealistic as they will lead to humping and decreased continuity. Further exploration of process parameter combinations in lower LED regime could shed light onto both the boundaries of this Cu Wt.% measurement as well as its reproducibility.

Conclusion

In the present study CuCrZr single tracks were successfully fabricated on IN718 substrate using PBF-LB/M. Both morphology and composition of the tracks were characterized. Main conclusions are as follows:

- Process parameter window, based primarily on the literature analysis, for printing CuCrZr on IN718 substrate revealed a predominant keyhole mode. From the analyzed process window, the results obtained for P_{Laser}= 500W, v_{Scan}=1000mm/s and d=60µm have been identified as the best trade-off between meltpool depth, width and a Cu Wt.% of 39.70±0.3.
- EDS mapping was identified as a reliable method to assess the effect of laser parameters on the melting of Cu powder, which is known to be notoriously challenging to melt via laser-based AM methods. A direct relationship between Cu Wt.% and *d* exist, but stalls at 60µm for LEDs above 0.8J/mm and no significant increment was visible between 60 and 90µm. The highest concentration of Cu obtained was 43.07% for 0.5J/mm, which coincides with process parameters for conduction mode.
- The distribution of Cu throughout the melt pool cross section is heavily affected by the energy transmission mode. It was shown that Cu is concentrating in the top parts of the melt pools in keyhole mode, while in conduction mode the distribution is more homogenous. Many of the process parameters chosen for the study still fall into the keyhole regime suggesting the need to cover a process parameter window below 0.5J/mm, or specifically within the energy conduction regime, to further clarify how both laser power and scanning speed affect the location of the Cu alloy. Informed by the initial assessment of the role of linear energy density (LED) in the multi-material interface formation and CuCrZr retention on the surface of the IN718 substrates, future work will be focus on the continuing optimization of the processing window to enable reliable and defect-free fabrication of multi-track and multi-layer CuCrZr-IN718 parts for enhanced microstructural and mechanical properties evaluation.

Acknowledgments

This research is conducted under the REDI Program, a project that has received funding from the European Union's Horizon 2020 research and innovation programme under the Marie Skłodowska-Curie grant agreement no. 101034328. This paper reflects only the author's view and the Research Executive Agency is not responsible for any use that may be made of the information it contains. The authors acknowledge the scientific and technical support of the RMIT Advanced Manufacturing Precinct and the RMIT RMMF microscopy facility.

References

(1) P. Gradl, C. Protz, S. Greene, D. Ellis, B. Lerch, and I. Locci, *Development and Hot-fire Testing of Additively Manufactured Copper Combustion Chambers for Liquid Rocket Engine Applications*. 2017. doi: 10.2514/6.2017-4670.

(2) P. Gradl, S. Greene, and T. Wammen, *Bimetallic Channel Wall Nozzle Development and Hot-fire Testing Using Additively Manufactured Laser Wire Direct Closeout Technology*. 2019. doi: 10.2514/6.2019-4361.

(3) P. R. Gradl, T. W. Teasley, C. S. Protz, M. B. Garcia, D. Ellis, and C. Kantzos, 'Advancing GRCop-based Bimetallic Additive Manufacturing to Optimize Component Design and Applications for Liquid Rocket Engines', in *AIAA Propulsion and Energy 2021 Forum*, VIRTUAL EVENT: American Institute of Aeronautics and Astronautics, Aug. 2021. doi: 10.2514/6.2021-3231.

(4) B. Blakey-Milner *et al.*, 'Metal additive manufacturing in aerospace: A review', *Mater. Des.*, vol. 209, p. 110008, Nov. 2021, doi: 10.1016/j.matdes.2021.110008.

(5) P. Gradl, C. Protz, D. Ellis, and S. Greene, *Progress in Additively Manufactured Copper-Alloy GRCop-84, GRCop-42, and Bimetallic Combustion Chambers for Liquid Rocket Engines*. 2019.

(6) 'ISO/ASTM TR 52912:2020', ISO. Accessed: Mar. 25, 2024. (Online). Available: https://www.iso.org/standard/71905.html

(7) M. Schneck, M. Horn, M. Schmitt, C. Seidel, G. Schlick, and G. Reinhart, 'Review on additive hybrid- and multi-material-manufacturing of metals by powder bed fusion: state of technology and development potential', *Prog. Addit. Manuf.*, vol. 6, no. 4, pp. 881–894, Dec. 2021, doi: 10.1007/s40964-021-00205-2.

(8) S. Mao, B. Yang, G. Liu, G. Liu, and Z. Zhang, 'Temperature distribution and residual stress evolution at the interface of CuCrZr/316 L multi-material by laser powder bed fusion', *Opt. Laser Technol.*, vol. 163, p. 109355, Aug. 2023, doi: 10.1016/j.optlastec.2023.109355.

(9) I. Meyer, M. Oel, T. Ehlers, and R. Lachmayer, 'Additive Manufacturing of Multi-Material Parts – Design Guidelines for Manufacturing of 316l/Cucrzr in Laser Powder Bed Fusion'. Rochester, NY, Feb. 05, 2023. doi: 10.2139/ssrn.4348515.

(10) L. Deillon, N. Abando Beldarrain, X. Li, and M. Bambach, 'Coupling hot isostatic pressing and laser powder bed fusion: A new strategy to manufacture defect-free CuCrZr-316L steel multi-material structures', *Mater. Des.*, vol. 241, p. 112914, May 2024, doi: 10.1016/j.matdes.2024.112914.

(11) T. Schroeder *et al.*, 'Transition zone parameter development in multi-material powder bed fusion: a general approach', *Prog. Addit. Manuf.*, May 2024, doi: 10.1007/s40964-024-00663-4.

(12) C. Pereira Martendal, P. D. Borges Esteves, L. Deillon, F. Malamud, J. F. Löffler, and M. Bambach, 'Effects of Beam Shaping on Copper-Steel Interfaces in Multi-Material Laser Powder Bed Fusion'. Rochester, NY, Dec. 22, 2023. doi: 10.2139/ssrn.4673732.

(13) S. Mao, D. Z. Zhang, Z. Ren, G. Fu, and X. Ma, 'Effects of process parameters on interfacial characterization and mechanical properties of 316L/CuCrZr functionally graded material by selective laser melting', *J. Alloys Compd.*, vol. 899, p. 163256, Apr. 2022, doi: 10.1016/j.jallcom.2021.163256.
(14) A. Marques, Â. Cunha, M. Gasik, O. Carvalho, F. S. Silva, and F. Bartolomeu, 'Inconel 718–copper parts fabricated by 3D multi-material laser powder bed fusion: a novel technological and designing approach for rocket engine', *Int. J. Adv. Manuf. Technol.*, vol. 122, no. 3, pp. 2113–2123, Sep. 2022, doi: 10.1007/s00170-022-10011-x.
(15) A. Marques, B. Guimarães, M. Cerqueira, F. Silva, and O. Carvalho, 'Multi-Material Inconel 718 Parts with Highly Conductive Copper Cooling Channels for Aerospace Applications', *Adv. Eng. Mater.*, vol. 25, no. 6, p. 2201349, 2023, doi: 10.1002/adem.202201349.
(16) Z. Li *et al.*, 'Selective laser melting of 316L–CuCrZr bimetallic structure via IN718 transition layer', *J. Mater. Res. Technol.*, vol. 25, pp. 3819–3834, Jul. 2023, doi: 10.1016/j.jmrt.2023.06.196.
(17) B. Onuike, B. Heer, and A. Bandyopadhyay, 'Additive manufacturing of Inconel 718—Copper alloy bimetallic structure using laser engineered net shaping (LENS^{TM})', *Addit. Manuf.*, vol. 21, pp. 133–140, May 2018, doi: 10.1016/j.addma.2018.02.007.
(18) T. M. Wischeropp, H. Tarhini, and C. Emmelmann, 'Influence of laser beam profile on the selective laser melting process of AlSi10Mg', *J. Laser Appl.*, vol. 32, no. 2, p. 022059, May 2020, doi: 10.2351/7.0000100.
(19) J. Grünewald, F. Gehringer, M. Schmöller, and K. Wudy, 'Influence of Ring-Shaped Beam Profiles on Process Stability and Productivity in Laser-Based Powder Bed Fusion of AISI 316L', *Metals*, vol. 11, no. 12, Art. no. 12, Dec. 2021, doi: 10.3390/met11121989.
(20) C. Tenbrock *et al.*, 'Influence of keyhole and conduction mode melting for top-hat shaped beam profiles in laser powder bed fusion', *J. Mater. Process. Technol.*, vol. 278, p. 116514, Apr. 2020, doi: 10.1016/j.jmatprotec.2019.116514.
(21) 'Evolution of molten pool during selective laser melting of Ti–6Al–4V - IOPscience'. Accessed: Jun. 19, 2024. (Online). Available: https://iopscience.iop.org/article/10.1088/1361-6463/aaee04/meta
(22) M. Brandt, *Laser Additive Manufacturing- Materials, Design, Technologies and Applications*. 2016.
(23) S. A. Khairallah and A. Anderson, 'Mesoscopic simulation model of selective laser melting of stainless steel powder', *J. Mater. Process. Technol.*, vol. 214, no. 11, pp. 2627–2636, Nov. 2014, doi: 10.1016/j.jmatprotec.2014.06.001.
(24) 'Multiscale Modeling of Powder Bed–Based Additive Manufacturing | Annual Reviews'. Accessed: Jun. 19, 2024. (Online). Available: https://www.annualreviews.org/content/journals/10.1146/annurev-matsci-070115-032158
(25) L. Gargalis *et al.*, 'Determining processing behaviour of pure Cu in laser powder bed fusion using direct micro-calorimetry', *J. Mater. Process. Technol.*, vol. 294, p. 117130, Aug. 2021, doi: 10.1016/j.jmatprotec.2021.117130.
(26) Z. Kuai *et al.*, 'Selective laser melting of CuCrZr alloy: processing optimisation, microstructure and mechanical properties', *J. Mater. Res. Technol.*, vol. 19, pp. 4915–4931, Jul. 2022, doi: 10.1016/j.jmrt.2022.06.158.
(27) S. Mao, Z. Ren, G. Liu, and D. Z. Zhang, 'A Numerical Study of Processing Parameters and Their Effect on the Formation of Immiscible Multi-Material in Laser Powder Bed Fusion Processes'. Rochester, NY, Mar. 08, 2024. doi: 10.2139/ssrn.4752348.

Received June 30, 2024; Revised September 10, 2024; Accepted September 28, 2024